





# Study of phase separation phenomena in half-doped manganites with isovalent substitution of rare-earth cations on example of $\text{Sm}_{0.32}\text{Pr}_{0.18}\text{Sr}_{0.5}\text{MnO}_3$

A. I. Kurbakov , V. A. Ryzhov , V. V. Runov, E. O. Bykov, I. I. Larionov, and V. V. Deriglazov 

*Petersburg Nuclear Physics Institute named by B. P. Konstantinov of National Research Centre “Kurchatov Institute”, 1 Orlova roscha, Gatchina, Leningrad Region 188300, Russia*

C. Martin and A. Maignan 

*CRISMAT, Normandie Université, ENSICAEN, UNICAEN, CNRS, CRISMAT, 14000 Caen, France*



(Received 10 September 2019; revised manuscript received 14 November 2019; published 27 November 2019)

The effect of isovalent substitution of rare-earth cations on the phase separation in half-doped manganites was studied on the example of  $\text{Sm}_{0.32}\text{Pr}_{0.18}\text{Sr}_{0.5}\text{MnO}_3$  by high-resolution neutron powder diffraction, neutron beam depolarization, second-harmonic magnetic response, and magnetization and resistivity measurements from 4 K up to room temperature and higher. A structural phase transition from the orthorhombic  $Pbnm$  phase to a mixture of  $Pbnm$  and monoclinic  $P2_1/m$  phases was observed upon cooling. The magnetic ground state was found to be phase-separated into three magnetic phases emerging at different temperatures, viz., ferromagnetic (FM) and antiferromagnetic A and charge-ordered CE types. FM clusters arise far above room temperature in the orthorhombic phase and coalesce upon cooling to produce the long-range FM order below 250 K and to arrive at the percolative FM phase below 120 K. The A- and CE-type orders form in the monoclinic phase at the temperatures 200 K and 120 K, respectively. The Sm/Pr isovalent substitution qualitatively changes the phase separation and significantly increases its temperature range compared to the parent compounds. The results obtained give us knowledge of phase separation occurring in systems with strong electron correlations and extend opportunities for fine-tuning of their properties.

DOI: [10.1103/PhysRevB.100.184424](https://doi.org/10.1103/PhysRevB.100.184424)

## I. INTRODUCTION

Phase separation (PS) is a generic feature of rare-earth manganites doped with alkali-earth ions ( $R_{1-x}A_x\text{MnO}_3$ ) underlying their remarkable magnetic, transport, magnetocaloric, and other properties applicable in technology [1]. This tendency is especially pronounced in the vicinity of phase boundaries, both in temperature and doping, where the system becomes more unstable to PS. For certain doping levels  $x$ , magnetic and structural phases and their alternation with temperature may considerably differ depending on the particular  $R$  and  $A$  cations. For instance, in the region close to  $x = 0.5$ , Ca-based Sm, Pr, Nd, and La manganites exhibit antiferromagnetic (AF) charge-ordered-type (CE) insulating ground states whereas these manganites (except, maybe, with Nd [2] and Sm [3]) half-doped with Sr ions possess the more conductive AF A-type structure [2,4,5]. Generally,  $x = 0.5$  is a particular doping level in the manganite phase diagrams separating mainly FM underdoped ( $x < 0.5$ ) and AF overdoped ( $x > 0.5$ ) areas with different crystal structures. Changing the chemical pressure due to different ionic radii of Ca and Sr ions modifies local structural parameters such as the Mn-O bond distances and Mn-O-Mn bond angles, which, in turn, essentially determine magnetic and transport properties via variation of electron hopping integrals. Thus, a partial substitution of  $\text{Ca}^{2+}$  for  $\text{Sr}^{2+}$  or some other divalent cation with

the continuous shift of the average ionic radius of the  $A$  cation, the  $\text{Mn}^{3+}/\text{Mn}^{4+}$  ratio being fixed, enables wide-range gradual variation of the manganite characteristics and their fine-tuning for particular application needs [6]. Herewith, such isovalent substitution (IS) can be accompanied by specific PS as shown, e.g., for  $\text{Pr}_{0.5}\text{Ca}_{0.2}\text{Sr}_{0.3}\text{MnO}_3$  [7]. The IS approach adds and is alternative to the conventional  $A$ -cation doping by changing the  $\text{Mn}^{3+}/\text{Mn}^{4+}$  ratio. As IS implies a fixed concentration of charge carriers, it affects the manganite properties more subtly, only via variation of geometrical parameters, viz., the average cationic radius and the radius variance. Besides, in the vicinity of  $x = 0.5$ , it is reasonable to expect coexistence of several (more than two) magnetic phases in the state with structural PS.

A partial substitution of trivalent  $R$ -cations provides even wider possibilities as the row of lanthanides is much longer than the alkali-earth one. Among numerous examples is the manganite  $\text{La}_{0.15}\text{Sm}_{0.85}\text{MnO}_{3.1}$ , where coexistence of nanoscale superconductivity and a fluctuating AF spin-liquid state was suggested [8]. The IS of rare-earth ions provides also an additional degree of freedom for optimizing the magnetocaloric effect. Doping  $\text{La}_{0.7}\text{Ca}_{0.3}\text{MnO}_3$  with  $\text{Nd}^{3+}$  ions was shown to increase the magnetic entropy gain reaching the maximum in  $\text{La}_{0.5}\text{Nd}_{0.2}\text{Ca}_{0.3}\text{MnO}_3$  [9]. Similarly, the magnetocaloric effect in  $\text{Sm}_{0.55-y}\text{Pr}_y\text{Sr}_{0.45}\text{MnO}_3$  was found to be optimized at  $y = 0.1$  with the outlook of employing this compound in magnetic refrigerators [10].

The systematic rare-earth IS can be used as a means for deeper insight into the physics of doping and

\*deriglazov\_vv@pnpi.nrcki.ru

temperature phase transitions along with the concomitant PS. The role of Jahn-Teller (JT) polarons in the metal-insulator (MI) transition and formation of the charge-ordered (CO) state in half-doped manganites was specified via the study of  $(\text{Nd}_{0.125}\text{Sm}_{0.875})_{0.52}\text{Sr}_{0.48}\text{MnO}_3$  [11]. The proximity of  $(\text{La}_{1-y}\text{Pr}_y)_{0.7}\text{Ca}_{0.3}\text{MnO}_3$  to the MI and FM-AF transitions for  $y$  between 0.75 and 1 enabled us to involve efficiently a subtle resource of the oxygen isotope substitution to study these phase transitions and formation of the mesoscopic and large-scale PS state [12,13].

The object of the present study is the half-doped SmSr manganite with the partial substitution of  $\text{Pr}^{3+}$  for  $\text{Sm}^{3+}$  ions. The parent compound  $\text{Sm}_{0.5}\text{Sr}_{0.5}\text{MnO}_3$  and the opposite-side  $\text{Pr}_{0.5}\text{Sr}_{0.5}\text{MnO}_3$  differ noticeably in their temperature behavior. From neutron powder diffraction (NPD) in polycrystalline  $^{154}\text{Sm}_{0.5}\text{Sr}_{0.5}\text{MnO}_3$  [14], macroscopic PS emerges below  $T_{\text{PS}} = 135$  K in the form of FM and A-type AF structures, each with its own long-range orbital order and with the close Curie and Néel temperatures. Both phases have similar crystalline orthorhombic symmetry  $Pbnm$  differing in the unit cell parameters and reveal the coherent JT effect with no long-range CO. However, short-range lattice distortions observed by electron diffraction (ED) admit a certain local CO [4,14]. The cell parameters of the FM-ordered phase remain unchanged upon the transition whereas, in the AF phase, the unit cell becomes appreciably distorted. Below 75 K the PS stabilizes with a certain ground-state volume ratio of the phases. The transport properties also change upon cooling. Above  $T_{\text{PS}}$  the substance is an insulator with the conductivity of the small-polaron-hopping (SPH) type [14,15] while below  $T_{\text{MI}} = 50$  K the insulator behavior changes for the metallic one. The SPH mechanism implies that at rather high temperatures (exceeding half the Debye temperature) the lattice dynamics becomes strong enough to destroy coherency of the polaronic Bloch-type wave functions. As a result, the low-temperature polaron-band conductivity fails and, instead, the conductivity is determined by polaron hopping between the neighboring sites strongly mediated by the lattice dynamics. Below  $T_{\text{MI}}$  the magnetic field 7 T reduces the resistivity by several orders indicating colossal magnetoresistance (CMR). From the hysteretic behavior of the second-harmonic magnetic response (M2), FM metallic clusters were found to arise in the paramagnetic phase well above  $T_{\text{PS}}$  as a precursor of the macroscopic magnetoelectronic phase separation (MEPS) [14] playing a key role in CMR.

The polycrystalline  $\text{Pr}_{0.5}\text{Sr}_{0.5}\text{MnO}_3$  exhibits a quite different temperature evolution. In the high-temperature tetragonal  $I4/mcm$  crystal structure, a transition from the low-conductive paramagnetic to FM state, metallic in single crystals [16–18] or an insulator in polycrystals [4,19], occurs at  $T_C = 265$  K with no additional structural distortions. Upon further cooling, the insulator AF A-type phase arises below 175 K with the orthorhombic  $Fmmm$  crystalline symmetry. The coexistence of both phases was found in the interval 135–175 K [19], i.e., above  $T_{\text{PS}}$  for  $\text{Sm}_{0.5}\text{Sr}_{0.5}\text{MnO}_3$ . No long-range CO was noticed down to the helium temperature. An important suggestion was made from a comparison of the NPD and ED data that the crystal structure symmetry changed under an applied magnetic field of 1 T [19].

TABLE I. A-site average cationic radius and variance.

	$\langle r_A \rangle$ (Å)	$\sigma^2$ (Å <sup>2</sup> )
$\text{Sm}_{0.5}\text{Sr}_{0.5}\text{MnO}_3$	1.2210	$7.92 \times 10^{-3}$
$\text{Sm}_{0.32}\text{Pr}_{0.18}\text{Sr}_{0.5}\text{MnO}_3$	1.2295	$6.64 \times 10^{-3}$
$\text{Pr}_{0.5}\text{Sr}_{0.5}\text{MnO}_3$	1.2445	$4.29 \times 10^{-3}$

In contrast to the polycrystalline samples, no FM order was observed in the single-crystal  $\text{Sm}_{0.5}\text{Sr}_{0.5}\text{MnO}_3$  for all temperatures. Instead, the AF A-type structure below 120 K and the CE structure with the checkerboard charge- and orbital order (OO) below 80 K [3] or the local CO below 220 K and the A-type structure below 170 K [20] were suggested in such samples. A transition at 140 K from the FM to AF A-type phase with the crystal symmetry  $P2_1/n$  and the stripelike CO was observed in the single-crystal  $\text{Pr}_{0.5}\text{Sr}_{0.5}\text{MnO}_3$  [2]. These findings indicate that structural inhomogeneities inherent to polycrystals tend to suppress CO and to favor PS.

By replacing samarium with praseodymium, one can pass gradually from the Sm compound with  $T_C \leq T_N$  and the phase-separated metallic ground state to the Pr compound with  $T_C > T_N$  and the nonseparated insulator ground state, thus drastically affecting the magnetic and transport properties in a wide temperature range. Increases of  $T_C$  and the low-temperature resistivity were, indeed, observed in  $\text{Sm}_{0.5-y}\text{Pr}_y\text{Sr}_{0.5}\text{MnO}_3$  with increasing  $y$  [4]. In this way,  $T_C$  was suggested from magnetization measurements to exceed  $T_N$  for  $y \geq 0.15$  [4]. From magnetic and ED studies, the CO AF insulator state is induced at low temperature at  $y = 0.15$ . This state easily collapses into the FM metallic state under magnetic field favoring CMR as shown for  $y = 0.18$  [4]. In the present study, this particular composition,  $^{154}\text{Sm}_{0.32}\text{Pr}_{0.18}\text{Sr}_{0.5}\text{MnO}_3$ , was examined in more detail by high-resolution NPD, neutron beam depolarization, and M2 techniques supplemented with magnetization and resistivity measurements from 4 K up to room temperature and higher.

The properties of the manganites with the general formula  $\text{ABO}_3$  depend on the A-site average cationic radius  $\langle r_A \rangle$  and A-site cationic size mismatch characterized by the variance  $\sigma^2 = \sum x_i r_i^2 - \langle r_A \rangle^2$ , where  $x_i$  is the concentration of the  $i$ th A cation and  $r_i$  is its respective ionic radius. These quantities for the studied and parent compounds are presented in Table I. As far as Pr substitutes for Sm,  $\langle r_A \rangle$  increases whereas  $\sigma^2$  decreases. Both tendencies lead to an increase of the conduction bandwidth and, thus, favor ferromagnetism as was evidenced for the large variety of manganites [4,21]. This trend will be shown to hold also for  $\text{Sm}_{0.5-y}\text{Pr}_y\text{Sr}_{0.5}\text{MnO}_3$ .

For the intermediate  $y = 0.18$  IS level, the macroscopic magnetostructural PS is found to differ in content from the cases  $y = 0$  and 0.5 and to start at a higher temperature. Upon cooling, the low-symmetry, monoclinic, structural component with the A-type AF order segregates at  $\simeq 200$  K and below 150 K splits into A and CO CE magnetic phases while the long-range FM order stays in the persisting high-temperature orthorhombic phase. The  $y = 0.18$  composition being close to the onset of PS in the ground state causes particular conditions for MEPS. FM clusters are shown to emerge well above

room temperature and their concentration to increase rapidly upon cooling favoring occurrence of magnetoresistance. The clusters grow in size via coalescence and percolate below 150 K. Parameters characterizing the cluster system in the superparamagnetic regime were obtained from the M2 data processing with the formalism based on the Fokker-Planck equation [22,23].

This study complements our complex investigation of SmSr manganites [14,24–28].

In Sec. II preparation of the samples and the employed techniques with the experimental details are described. In Sec. III the obtained results are presented and discussed. Section IV contains the conclusion.

## II. EXPERIMENTAL

The sample  $^{154}\text{Sm}_{0.32}\text{Pr}_{0.18}\text{Sr}_{0.5}\text{MnO}_3$  for the neutron studies was synthesized using the isotope  $^{154}\text{Sm}$  to avoid strong absorption of neutrons due to a large abundance of  $^{149}\text{Sm}$  in the natural mixture of isotopes. The synthesis of Pr compounds requires precautions to produce a single-phase cubic perovskite without admixture of the hexagonal polytype (100). The stoichiometric amounts of  $^{154}\text{Sm}_2\text{O}_3$ ,  $\text{MnO}_2$ ,  $\text{SrCO}_3$ , and  $\text{Pr}_6\text{O}_{11}$  were carefully mixed and treated at 1270 K for 48 h with a few intermediate grindings to complete decarbonation. The obtained powder was pressed into the form of pellets and a synthesis was carried out at 1470 K and then at 1770 K for 12 h. After that the sample was slowly cooled down to 1070 K with a rate of 5 K/min followed by a quenching performed down to room temperature [14].

The neutron diffraction experiment was carried out with the 70-counter high-resolution powder diffractometer at the cold neutron guide of the reactor ORPHEE (LLB, Saclay, France) in the G4.2 position (now transferred to G4.4) [29]. The superposition regime of the data acquisition was employed for monochromatic neutrons with the wavelength  $\lambda = 0.23433$  nm in the angular range  $3^\circ \leq 2\theta \leq 174^\circ$  on warming from 1.5 K up to room temperature, the powder sample being inside a vanadium cylindrical holder 8 mm in diameter. The types of crystal and magnetic structures were identified and their parameters were extracted from the diffraction patterns by Rietveld refinement with the FULLPROF suite [30].

Neutron beam depolarization is known to be a powerful technique to study the media with FM inhomogeneities [24,31,32]. The neutron magnetic moment interacts with the internal magnetic field of an FM cluster. As the internal fields of different clusters are thermally disordered, the beam, passed through the cluster ensemble, depolarizes. The scattering on structural inhomogeneities does not affect the depolarization at all.

The neutron beam depolarization was measured at the small-angle polarized-neutron scattering facility VECTOR at the reactor WWR-M (Gatchina, Russia) enabling us to perform the polarization analysis for the momentum transfers  $0 < q < 3$  nm $^{-1}$  in the slit geometry. The incident beam had the mean neutron wavelength  $\lambda = 0.92$  nm, the spectrum half-width  $\Delta\lambda/\lambda = 0.25$ , and the polarization  $P_0 = 0.94$ . The measurements were performed in the temperature range 20–300 K and the magnetic field less than 10 Oe.

The second harmonic of the longitudinal component of the magnetization  $M_2$  was measured in the parallel dc and ac magnetic fields  $H + h \sin \omega t$  with the frequency  $f = \omega/2\pi = 15.7$  MHz and  $h \leq 35$  Oe to ensure the condition  $M_2 \propto h^2$ . The real  $\text{Re}M_2(H)$  and imaginary  $\text{Im}M_2(H)$  parts were simultaneously recorded as functions of the dc field, which was slowly scanned within  $\pm 300$  Oe symmetrically to  $H = 0$ . The temperature was varied by slow cooling and warming in the range 92–307 K with the stabilization time before recording the signal not less than 300 s for each temperature point. The experimental setup with the measurement sensitivity  $10^{-9}$  emu and the method of separation of the  $M_2$  phase components were described previously [33]. The sample in the form of a pressed polycrystalline plate with the mass 2 mg and the size  $1.2 \times 1.2 \times 0.2$  mm $^3$  was oriented along the fields.

The resistance of the sample was measured on a  $2 \times 2 \times 10$  mm $^3$  bar in zero magnetic field and in the field 7 T by the conventional four-probe technique on warming and cooling in the temperature range 5–400 K.

The magnetization was measured with a vibrating sample magnetometer IQ-3001 in the magnetic field 1.4 T on warming from 4.2 to 300 K after zero-field cooling.

## III. RESULTS AND DISCUSSION

### A. Neutron powder diffraction

The NPD patterns presented in Fig. 1 demonstrate temperature evolution of the crystal and magnetic structures on warming. The first most intense magnetic peaks (at low  $2\theta$  angles) correspond to FM and AF A-type and CE-type phases. As an example, the pattern for 1.5 K with its Rietveld refinement is shown in Fig. 2. At 300 K the crystal structure is described solely by the  $Pbnm$  space group whereas at the lower temperatures the NPD profiles can be well fitted only by adding one more crystal structure, with the monoclinic space group  $P2_1/m$ , the ion positions corresponding to the high-temperature phase. This is clearly seen on the fragment of the NPD pattern in the inset of Fig. 2. The (101)+(020) doublet, unresolved in the orthorhombic structure, is incapable of describing the experimental double peak, whereas in the monoclinic structure, this doublet is well resolved. While in the left experimental peak there is a contribution of both crystal phases plus a FM admixture to the orthorhombic component, the right peak corresponds to the purely monoclinic (020) reflex.

The structural parameters for the lowest and highest temperatures are presented in Table II. The lack of the mirror plane  $z = \frac{1}{4}$  in the monoclinic phase leads to two nonequivalent Mn positions along the  $c$  axis,  $\frac{1}{2}00$  and  $0\frac{1}{2}0$ , resulting in the layered order with the stacking of  $\text{MnO}_6$  octahedra of different sizes along the  $c$  axis. Additional O positions also appear. The temperature evolution of the structural phases is shown in Fig. 3(b). For comparison the temperature dependencies of the phase contents are presented also for the parent compounds  $\text{Sm}_{0.5}\text{Sr}_{0.5}\text{MnO}_3$  [Fig. 3(a)] [14] and  $\text{Pr}_{0.5}\text{Sr}_{0.5}\text{MnO}_3$  [Fig. 3(c)] [19]. These figures visualize the temperature behavior of the parent compounds as described in the Introduction. Upon cooling the amount of the high-temperature orthorhombic phase I gradually decreases

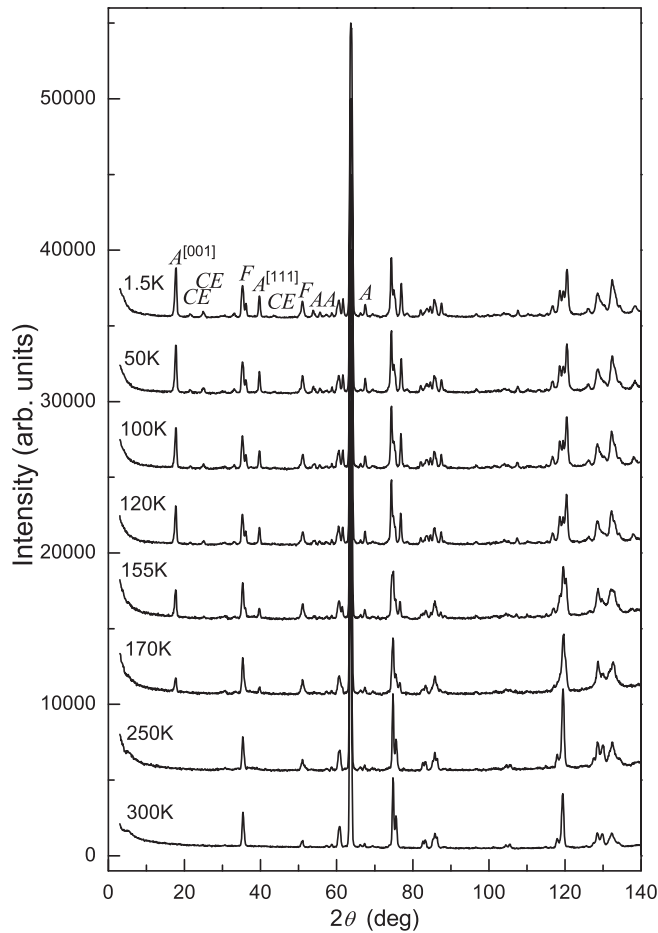


FIG. 1. NPD patterns of  $^{154}\text{Sm}_{0.32}\text{Pr}_{0.18}\text{Sr}_{0.5}\text{MnO}_3$ . The most intense magnetic peaks are marked corresponding to FM (F) and AF A-type and CE-type structures.

with the simultaneous growth of the monoclinic phase II [Fig. 3(b)]. By extrapolation, the onset of phase II  $T_{\text{PS}}$  may be localized at 200 K or, perhaps, somewhat lower despite the lack of experimental points in this temperature region, in agreement with the data of other measurements presented hereinafter. Below 110 K the phase ratio stabilizes at 0.25/0.75 with predominance of phase II while, in the parent compound  $^{154}\text{Sm}_{0.5}\text{Sr}_{0.5}\text{MnO}_3$ , this ratio stabilized below 75 K at the level 0.63/0.37 with prevalence of the high-temperature phase [Fig. 3(a)]. Thus, the PS tendency for the Pr-doped compound with  $y = 0.18$  is appreciably stronger than for the sample without IS. With Pr doping, the new phase II emerges at higher temperature and supplants the high-temperature phase I to a greater extent, the phase-ratio stabilization temperature increases, and the monoclinic angle  $\beta$  of phase II gradually deviates from  $90^\circ$ . It is reasonable to expect that, at some slightly larger doping  $y$ , the new phase II will completely replace phase I at low temperatures resulting in a non-PS ground state but even wider PS temperature range. Upon further increase of  $y$  toward 0.5, the temperature of the upper PS boundary is expected to decrease with changing the crystalline symmetries of both phases to arrive at  $\text{Pr}_{0.5}\text{Sr}_{0.5}\text{MnO}_3$  [Fig. 3(c)].

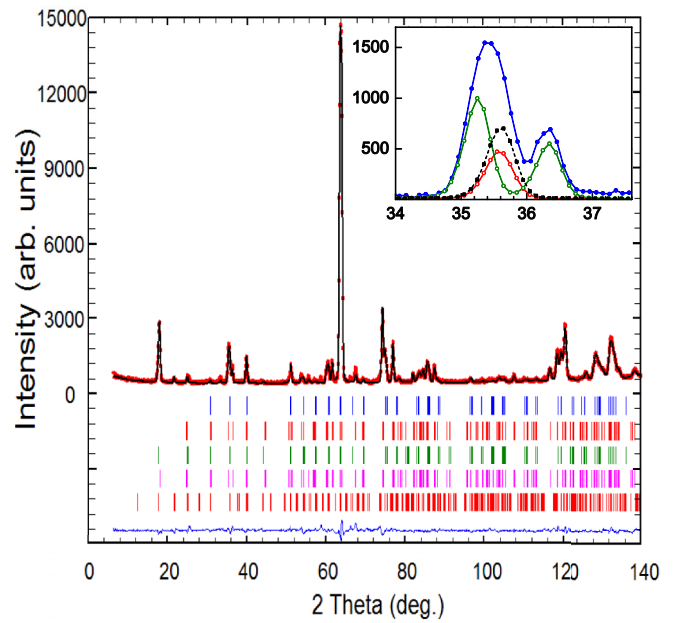


FIG. 2. Rietveld refinement of the NPD pattern for 1.5 K: experiment (symbols) and calculation (continuous line). Bragg peaks are marked with vertical ticks (top to bottom): crystal  $Pbnm$  and  $P2_1/m$ , as well as FM and AF A-type and CE-type structures; the bottom curve is the remainder of experiment minus calculation. Inset: a fragment of the measured NPD pattern (blue filled circles), which is a superposition of three calculated contributions, viz., orthorhombic (red open circles) corresponding to the unresolved doublet  $(101)+(020)$   $2\theta = 35.52^\circ + 35.69^\circ$ , monoclinic (green open circles) corresponding to the resolved reflexes  $(101)$   $2\theta = 35.29^\circ$  and  $(020)$   $2\theta = 36.33^\circ$ , and FM admixture (black filled rectangles with dashed line). Axis coordinates are the same as in the main plot.

The Mn-O-Mn angles in both phases are almost independent of temperature. The apical and equatorial angles,  $162^\circ$  and  $167^\circ$ , respectively, are quite close for both structures unlike the Mn-O distances (Table II) and the lattice constants [Fig. 4(a)]. In both phases I and II,  $c\sqrt{2} < b < a$ . However, while phase I exhibits a small difference between its lattice parameters only slightly varying with temperature, phase II reveals monoclinic distortions with noticeable contraction along the  $c$  axis. These distortions and the monoclinic angle  $\beta$  rise upon cooling while the unit cell volumes decrease for both structures [Fig. 4(b)].

Distinction between the interatomic distances Mn-O (Table II) in each structure indicates cooperative JT distortions of  $\text{MnO}_6$  octahedra. In the orthorhombic phase, the distortions are small, with the apical bond distance Mn-O1 lying between the equatorial bond distances Mn-O2 below 300 K. In contrast, the octahedrons of the monoclinic phase are appreciably shrunk in the apical direction while the equatorial bond lengths differ from each other to a much lesser extent (Table II). The latter is fairly consistent with the JT mode  $Q_3 = 2\Delta_z - \Delta_x - \Delta_y$  with the  $Q_3/Q_2$  mixing angle close to  $\pi$ , where  $\Delta_{x,y}$  and  $\Delta_z$  are the distortions of the equatorial and apical oxygen ions, respectively [1]. This corresponds to the  $d_{x^2-y^2}$  OO with  $e_g$  electrons localized predominantly in the  $ab$  plane.

TABLE II. Structural parameters of  $\text{Sm}_{0.32}\text{Pr}_{0.18}\text{Sr}_{0.5}\text{MnO}_3$  from NPD for the lowest and highest temperatures and  $R$  factors.

	$T = 1.5$ K		$T = 300$ K
	$Pbnm$ (25%)	$P2_1/m$ (75%)	$Pbnm$ (100%)
$a$ (Å)	5.4445(9)	5.5001(3)	5.4641(3)
$b$ (Å)	5.4211(7)	5.4473(3)	5.4308(2)
$c$ (Å)	7.6478(9)	7.5178(4)	7.6366(2)
$c/\sqrt{2}$ (Å)	5.4078	5.3159	5.3999
$\beta$ (deg)		90.13(1)	
$V_0$ (Å <sup>3</sup> )	225.73(9)	225.24(4)	226.61(3)
Mn1:			
$x_1$	0.5	0.5	0.5
$y_1$	0	0	0
$z_1$	0	0	0
Mn2:			
$x_2$		0	
$y_2$		0.5	
$z_2$		0	
Sm, Pr, Sr1:			
$x_1$	-0.0024(7)	-0.0024	0.0014(6)
$y_1$	-0.010(2)	-0.010	-0.0093(2)
$z_1$	0.25	0.25	0.25
Sm, Pr, Sr2:			
$x_2 = 1/2 - x_1$		0.5024	
$y_2 = 1/2 + y_1$		0.49	
$z_2 = z_1$		0.25	
O1:			
$x_1$	0.0560(9)	0.0560	0.0543(8)
$y_1$	0.501(3)	0.501	0.507(2)
$z_1$	0.25	0.25	0.25
O11:			
$x_{11} = 1/2 - x_1$		0.444	
$y_{11} = 1/2 + y_1$		0.001	
$z_{11} = z_1$		0.25	
O2:			
$x_2$	-0.238(1)	-0.238	-0.2382(8)
$y_2$	0.240(1)	0.240	0.2615(9)
$z_2$	0.0278(4)	0.0278	-0.0255(3)
O22:			
$x_{22} = 1/2 - x_2$		0.738	
$y_{22} = 1/2 + y_2$		0.740	
$z_{22} = z_2$		0.0278	
Interatomic distances (Å):			
Mn-O1	$2 \times 1.9361(8)$	1.9046(8)	$2 \times 1.9324(7)$
		1.9046(8)	
Mn-O21	$2 \times 1.942(6)$	1.955(6)	$2 \times 1.940(5)$
		1.959(6)	
Mn-O22	$2 \times 1.926(6)$	1.942(6)	$2 \times 1.936(5)$
		1.938(6)	
Interbond angles (deg):			
Mn-O1-Mn	161.87(4)	161.34(4)	162.21(3)
		161.34(4)	
Mn-O2-Mn	166.5(3)	166.7(3)	167.3(2)
		166.8(3)	
$R_p$		4.47	3.74
$R_{wp}$		6.35	5.37
$R_{exp}$		2.63	2.56
$R_b$	3.56	4.37	4.64
$R_m$	8.17	12.7, 30.4	

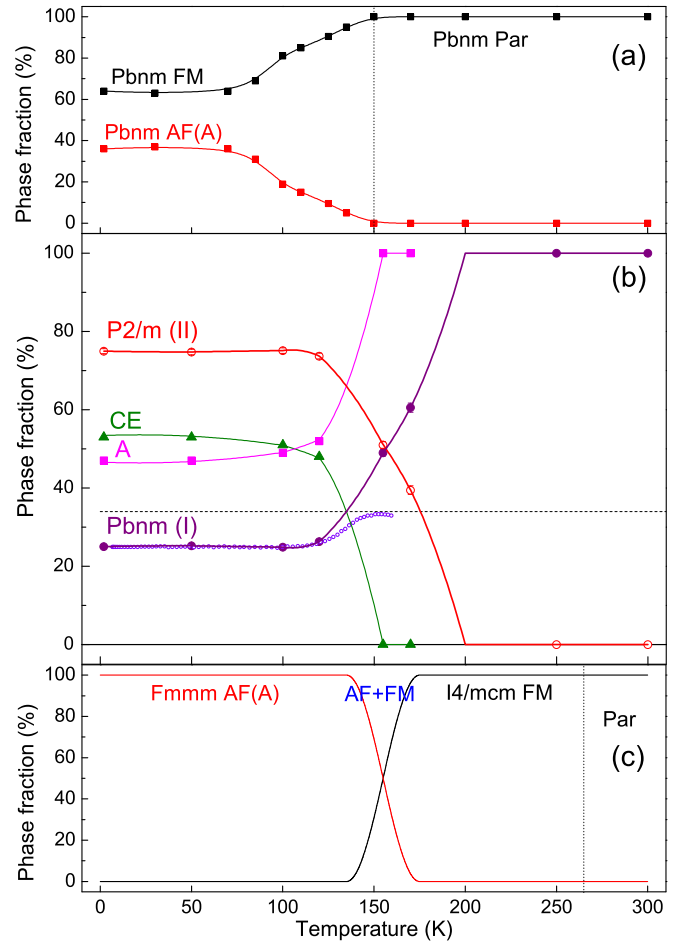


FIG. 3. (a) Volume fractions of phases vs temperature for  $\text{Sm}_{0.5}\text{Sr}_{0.5}\text{MnO}_3$  as obtained in Ref. [14]. (b) Volume fractions of the orthorhombic (I) and monoclinic (II) crystal phases (circles) for  $\text{Sm}_{0.32}\text{Pr}_{0.18}\text{Sr}_{0.5}\text{MnO}_3$ , as well as of A and CE magnetic structures in the monoclinic crystal phase (rectangles and triangles, respectively) vs temperature traced with guides for the eye. The horizontal broken line is an approximate percolation threshold for FM clusters corresponding to randomly distributed spheres. Small circles are recovery of the FM phase fraction from magnetization measurements (Fig. 5). (c) Volume fractions of phases vs temperature for  $\text{Pr}_{0.5}\text{Sr}_{0.5}\text{MnO}_3$  schematically recovered from NPD data of Ref. [19].

From the NPD patterns (Fig. 1), the sample exhibits macroscopic magnetic PS into FM and two AF phases of A and CE types. The long-range FM order arises somewhat above 250 K in the orthorhombic phase, well above  $T_{PS}$ , and persists down to the lowest temperatures. The FM order may be ascribed only to phase I as among the well-resolved peaks of the two crystal phases only the peaks of the orthorhombic phase exhibit appreciable temperature dependence due to the FM contribution. This is clearly seen in the angular regions  $2\theta = 35^\circ\text{--}37^\circ$  for the doublet  $[110] + [002]$  and  $50^\circ\text{--}52^\circ$  for the triplet  $[200] + [020] + [112]$  and demonstrated in more detail in the inset to Fig. 2. The FM order goes on extending over the orthorhombic crystal phase upon cooling until its saturation at 120 K as further seen from the magnetization measurements.

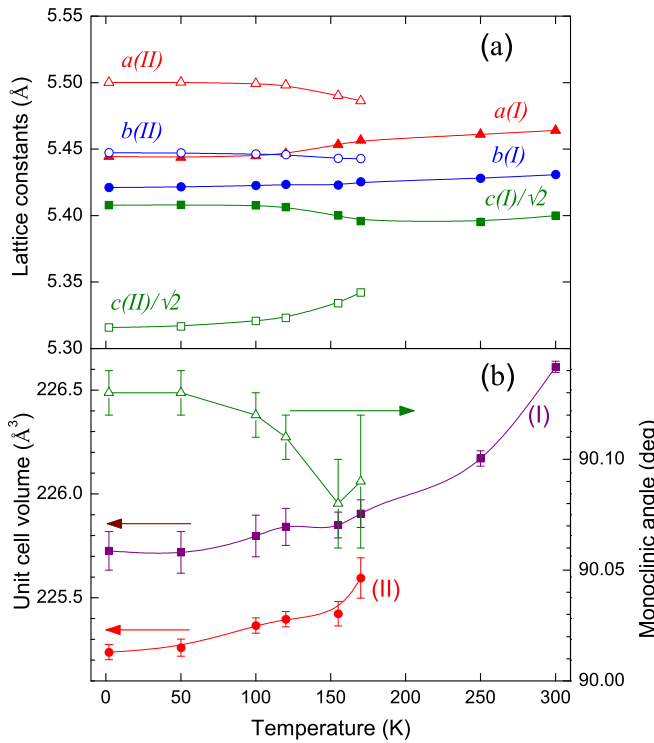


FIG. 4. Temperature dependencies of (a) lattice constants for the orthorhombic (I) (solid symbols) and monoclinic (II) (open symbols) crystal phases, and (b) corresponding unit cell volumes (filled symbols) and the monoclinic angle  $\beta$  of phase II (open triangles). Lines are guides for the eye.

The AF A-type order was found for the monoclinic phase as seen from the angular positions of the first, most intense, [001] and [111] A peaks (Fig. 1). Within the double-exchange model, this magnetic order is consistent with the  $d_{x^2-y^2}$  OO. Below 150 K the A structure partially converts into the AF CE structure with the  $d_{3x^2-r^2}/d_{3y^2-r^2}$  OO and Mn-ion magnetic moments oriented along the  $c$  axis. The CE structure is also related to the monoclinic crystal phase as its two nonequivalent Mn-ion positions admit CO implying different distortions of the respective oxygen octahedra. Besides, the localization of  $e_g$  electrons in the  $ab$  plane is consistent with the observed shrinking of the octahedra along the  $c$  axis. The volume fraction of the two structures is close to 1:1 with a small excess of the CE component at low temperatures [Fig. 3(b)].

The temperature behavior of Mn-ion magnetic moments for the FM and both AF structures extracted from the NPD patterns is presented in Fig. 5. The difference in the Mn magnetic moments of the CE phase due to the charge ordering  $\text{Mn}^{3+}/\text{Mn}^{4+}$  was disregarded. Upon cooling the magnetic moments rise and reach the maxima 3.66, 2.78, and 2.60  $\mu_B$  for FM, CE, and A structures, respectively. The FM moments were obtained assuming the whole orthorhombic phase to be FM ordered.

As seen in Fig. 5, the NPD FM moment exists already at 250 K, well above  $T_{PS}$ , additionally evidencing the belonging of FM order to the orthorhombic phase. Due to the cluster growth upon cooling, the size of some FM clusters and their concentration at this temperature become large enough to be

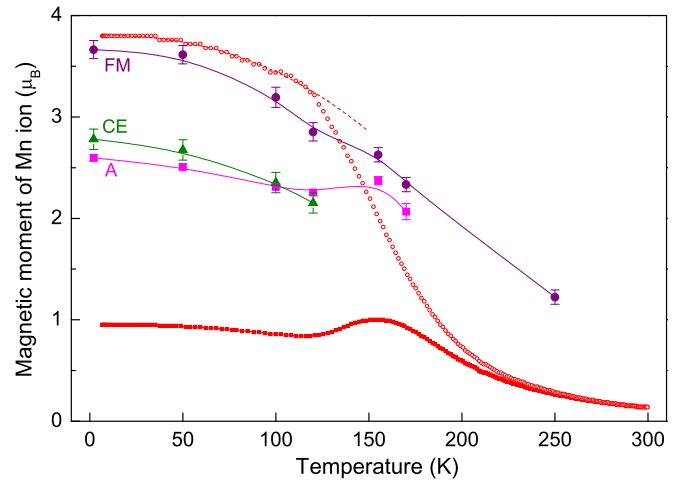


FIG. 5. Temperature dependencies of Mn magnetic moments for FM (circles), CE (triangles), and A (squares) structures (from NPD data) traced with guides for the eye and for magnetization measured in 1.4 T applied magnetic field on warming after ZFC (small solid circles) and calculated per Mn ion, and this magnetization normalized by the volume fraction of phase I [Fig. 3(b)] (small open circles) with its fit by Eq. (1) (broken line).

detected by NPD as a long-range FM order. This may be considered as an onset of the macroscopic magnetoelectronic PS (see below).

## B. Magnetization data

In the same Fig. 5, the magnetization per Mn ion is presented as obtained from the measurement on warming in the field 1.4 T after zero-field cooling (ZFC). The low-temperature values are much smaller than those obtained from NPD for the FM phase as the measured magnetization is an average over the whole sample volume whereas the NPD FM moment refers only to the orthorhombic fraction. The magnetization exhibits a nonmonotonic behavior with the maximum at 160 K. This hump results from the competition between the increase of the phase I volume with temperature [Fig. 3(b)] and the reduction of the ferromagnetic component above 120 K. The maximum is located in the  $T$  region of the steepest growth of the phase I fraction. The magnetization persists up to the room temperature and well above evidencing the magnetically inhomogeneous (and, mainly, short-ordered as there is no signature in NPD patterns) character of the sample. From nonlinear magnetic response (Sec. III E), MEPS in the form of FM clusters dispersed in the paramagnetic matrix occurs as precursor of the long-range FM order additionally stimulated by applying magnetic field.

The magnetization renormalized by the concentration of the orthorhombic phase is close to the magnetic moments obtained from NPD at low temperatures indicating this crystal phase to be totally ferromagnetic below 120 K (Fig. 5). The renormalization recovers the expected monotonic behavior of the magnetization. A small excess of the magnetization over the NPD magnetic moments is due to slight magnetization of the AF phases by the applied magnetic field. Incidentally, the field 1.4 T is still insufficient to convert the CE into FM order.

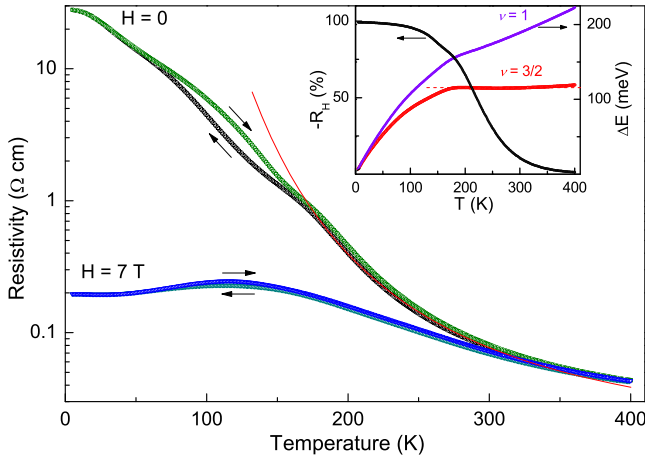


FIG. 6. Temperature dependencies of the resistivity measured in zero magnetic field and in 7 T on cooling and heating with the best fit by Eq. (2) (red curve). Inset: magnetoresistance (black) and activation energy  $\Delta E$  vs temperature [Eq. (3)] for the adiabatic ( $\nu = 1$ , violet) and nonadiabatic ( $\nu = 3/2$ , red) regimes.

The variation of the magnetization below 120 K may be well described *phenomenologically* by the power law

$$M(T) = M_0 \left[ 1 - \left( \frac{T}{T_0} \right)^\kappa \right] \quad (1)$$

with  $M_0 = 3.8 \mu_B$ ,  $T_0 = 277$  K, and  $\kappa = 2.3$ . Such a form of  $T$  dependence is inherent to some types of FM spin dynamics, e.g., the Heisenberg spin waves ( $\kappa = 3/2$ ) and Stoner excitations in metallic ferromagnets ( $\kappa = 2$ ) [34]. The parameters of Eq. (1) may also depend on magnetic field. The deviation of the renormalized magnetization from the fit curve above 120 K is due to incomplete filling of phase I by FM order. It is reasonable to assume that the magnetization of the FM phase itself follows Eq. (1) also at a little higher temperatures. With this assumption, the fraction of the FM phase was evaluated as presented in Fig. 3(b). Its value reaches a maximum at 160 K, close to but not exceeding the percolation threshold, in agreement with the insulator transport properties (Sec. III C).

### C. Transport properties

The manganite under study reveals the insulator temperature behavior in the whole temperature range measured (Fig. 6). The SPH conductivity is found above 180 K described by the general formula for the resistivity

$$\rho = \rho_0 T^\nu \exp\left(\frac{\Delta E}{T}\right), \quad (2)$$

where  $\nu = 1$  or  $3/2$  corresponds to the adiabatic or nonadiabatic limits, respectively [15,35,36]. To differentiate between these two cases, the activation energy

$$\Delta E = T \ln\left(\frac{\rho}{\rho_0 T^\nu}\right) \quad (3)$$

is built as a function of temperature for the two  $\nu$  values (inset in Fig. 6). In the case  $\nu = 3/2$ , the activation energy  $\Delta E = 1343$  K is independent of temperature above 180 K unlike the case  $\nu = 1$ , thus evidencing the nonadiabatic SPH

regime. This regime, unlike the adiabatic one, implies that electrons are unable to follow rapid fluctuations of the lattice and to hop from one site to another in the most favorable moment when the local distortion patterns for the two sites are the same [15]. The SPH conductivity model is valid for  $T \gtrsim \Theta_D/2$ , where  $\Theta_D$  is the Debye temperature. The estimation  $\Theta_D \leq 360$  K is realistic for doped manganites [37]. The same type of resistivity behavior was observed also in  $\text{Sm}_{0.5}\text{Sr}_{0.5}\text{MnO}_3$  above 140 K with the close activation energy  $\Delta E = 1440$  K [14].

Upon cooling below 180 K, the SPH regime is violated by the crystalline PS, which is accompanied by partial transfer of electrons from the monoclinic to orthorhombic phase. Indeed, accumulation of electrons in FM clusters leaves the paramagnetic matrix of phase I positively charged. The electron depletion of the matrix increases with the cluster growth upon cooling. Electrons passing from phase II to the electron-deficient matrix of phase I tend to smoothen the inhomogeneous spatial distribution of the electron density to decrease the Coulomb energy. The replenishment of the phase I matrix with electrons facilitates the cluster growth ensuring additional gain in the double-exchange kinetic energy. Both tendencies reduce the total energy. The electron depletion of phase II favors occurrence of the AF A structure typical for the doping  $x > 0.5$  whereas the enrichment of phase I with electrons shifts it to the doping  $x < 0.5$  enhancing the FM tendency. As the doping  $x = 0.5$  exactly separates these two magnetic states [1,4], even a small shift in  $x$  stabilizes either FM or AF state. Thus, the crystalline PS occurs along with the macroscopic MEPS. The two crystal phases have different transport properties. The monoclinic phase with its large  $Q_3$ -type JT distortions is more resistive than the orthorhombic phase with much smaller JT distortions and large clusters with metallic conductivity. The increase of the conductivity of phase I dominates over the conductivity decrease of phase II resulting in the deviation from the SPH regime of the whole sample toward lower resistivity (Fig. 6). The distinction between  $T_{PS}$  (200 K) and the temperature of the SPH regime failure can be due to the fact that the powder sample was additionally sintered to make it available for the resistivity measurements. However, despite the precautions some modification, probably, occurred.

A similar scenario, probably, occurs in  $\text{Sm}_{0.5}\text{Sr}_{0.5}\text{MnO}_3$ , where the onset of the crystalline PS and the breakdown of the SPH regime were found to occur at close temperatures inside the narrow interval 135–150 K [14].

M2 measurements offer additional evidence to this PS scenario (Sec. III E). In particular, the sharp enhancement of the cluster growth stimulated by the structural transition will be shown to result in percolation of clusters. The hysteresis of the zero-field resistivity at the temperatures  $70 < T < 150$  K (Fig. 6) is just indicative of the first-order phase transition, where “infinite” FM conductive clusters arise upon cooling inside the regions occupied by the crystal phase I. Such regions may coincide with crystallites. However, the percolation does not result in the metal conductivity of the whole sample as the fraction of the phase I regions itself at such temperatures is already not large enough for percolation between the regions [Fig. 3(b)]. At the onset of the FM percolation inside the phase I regions, the growing poorly conductive monoclinic phase II occupies already 60% of the sample volume [Fig. 3(b)].

The CO of the CE magnetic structure additionally contributes to the insulator character of this crystal phase.

Under the applied magnetic field, the resistivity decreases revealing CMR below the room temperature (Fig. 6). The field 7 T stimulates intensive growth of conductive FM regions. The magnetoresistance  $R_H = [\rho(7\text{ T}) - \rho(0)]/\rho(0)$  grows with cooling (inset in Fig. 6) upon evolution of MEPS. As below 120 K the whole orthorhombic phase becomes ferromagnetic, the MEPS stabilizes, and CMR should be expected to vanish. However, not only the magnetoresistance continues to increase but also at 120 K the insulator behavior changes for the metallic one. The reason is that under magnetic field the appeared CE phase transforms into the FM state, thus increasing the fraction of conductive regions. A slightly discernible inflection on the  $R_H(T)$  curve at 150 K is an indication of turning on this CMR mechanism. This additional contribution turns out to be sufficient to exceed the percolation threshold and to provide metallicity of the sample at the field 7 T.

It may seem surprising that the temperature dependence for the SPH conductivity [Eq. (2)] is not violated by the effect of grain boundaries in the wide range above  $T_{PS}$ . However, such a  $T$  dependence exclusively characterizes the SPH mechanism and Fig. 6, especially the inset, unambiguously evidences validity of this model. In particular, the variable range hopping (VRH) model noticeably disagrees with the measured resistivity. This finding leads to the suggestion that the grain boundaries contribute to the sample conductivity only via renormalization of  $\rho_0$  in Eq. (2) not affecting the temperature dependence itself. Though such a behavior is not common for manganites, somewhat similar features were observed in compounds with a different type of conductivity. For instance, resistivity of  $\text{Nd}_{0.7}\text{Ba}_{0.3}\text{MnO}_3$  exhibits VRH temperature behavior above  $T_C$  identical for single-crystal and ceramic samples, while it is quite different at lower temperatures [38].

#### D. Neutron beam depolarization

Figure 7 shows temperature dependencies of the neutron beam polarization on passing the samples of  $\text{Sm}_{0.32}\text{Pr}_{0.18}\text{Sr}_{0.5}\text{MnO}_3$  and parent  $\text{Sm}_{0.5}\text{Sr}_{0.5}\text{MnO}_3$ , both 2 mm thick, as well as the sum of nuclear and magnetic scattering intensities for the former. An increase of the concentration and size of FM clusters induces the rise of depolarization. The polarization behaviors for the two compounds considerably differ. Depolarization in  $\text{Sm}_{0.32}\text{Pr}_{0.18}\text{Sr}_{0.5}\text{MnO}_3$  becomes visible just below 300 K whereas  $\text{Sm}_{0.5}\text{Sr}_{0.5}\text{MnO}_3$  depolarizes the beam at much lower temperatures, below 115 K, and in the shorter temperature interval. This observation suggests that additional disorder brought in by Pr/Sm IS essentially destabilizes the system stimulating the occurrence of FM inhomogeneities.

Below  $T_{PS}$  the decrease of the polarization in  $\text{Sm}_{0.32}\text{Pr}_{0.18}\text{Sr}_{0.5}\text{MnO}_3$  becomes even steeper. Redistribution of electrons between the two crystal phases stimulates occurrence of macroscopically large clusters in phase I resulting in (i) enhancement of the depolarization rise and (ii) emergence of refraction of neutrons on their boundaries seen

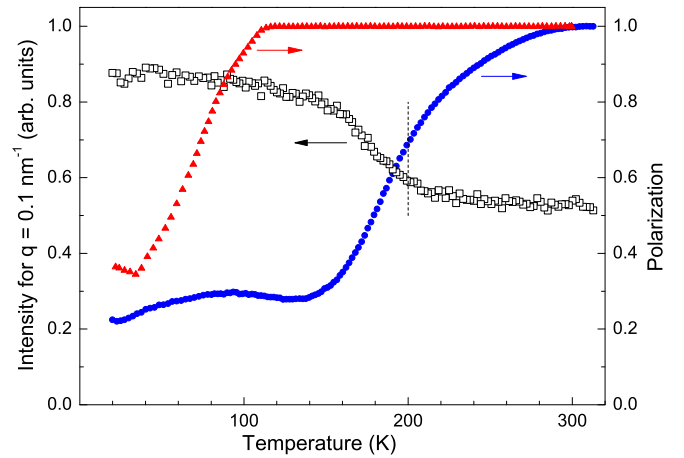


FIG. 7. Temperature dependencies of the neutron beam polarization for  $\text{Sm}_{0.5}\text{Sr}_{0.5}\text{MnO}_3$  (triangles) and  $\text{Sm}_{0.32}\text{Pr}_{0.18}\text{Sr}_{0.5}\text{MnO}_3$  (circles), and scattering intensity at the momentum transfer  $q = 0.1\text{ nm}^{-1}$  (open squares) for  $\text{Sm}_{0.32}\text{Pr}_{0.18}\text{Sr}_{0.5}\text{MnO}_3$ ; the dotted line marks  $T_{PS}$ .

in Fig. 7 as an increase of the scattering intensity. The M2 measurements further corroborate this finding (Sec. III E).

Below 140 K the polarization exhibits a nonmonotonic temperature behavior determined by two mutually opposing tendencies. Percolation in the phase I crystallites and their filling with the FM phase magnetically homogenizes the sample decreasing the depolarization effect. At the same time, the extending FM phase experiences formation of domains increasing the depolarization. Besides, the magnetization itself increases upon cooling due to weakening of the FM spin dynamics (Fig. 5). This leads to the raise of the magnetic field inside clusters enhancing depolarization. The domain formation gives the major effect. Among these tendencies, the homogenizing is active and prevails above 100 K while at lower temperatures the domain contribution completely dominates.

#### E. Nonlinear magnetic response

In Fig. 8 the dc-field direct and reverse scans for real and imaginary parts of the second-harmonic magnetic response are presented for three characteristic temperatures. Already at the highest measured temperature, a clear signal from magnetic inhomogeneities is observed suggesting their formation well above the room temperature. The upper panels 306 K exemplify the type of the response inherent to the region from the highest measured temperature 307 K down to 300 K. These nonhysteretic patterns with well-expressed extrema and opposite signs of the real and imaginary parts are typical for superparamagnetic clusters arising due to microscopic MEPS observed in the large variety of doped manganites and cobaltites [32,39–41]. The  $H$  antisymmetry of the patterns stems from common symmetry requirements for the second harmonic. At these temperatures, the signal rapidly rises upon cooling (Fig. 9) with retaining its form. This type of the temperature dependence denotes a growth of the concentration of clusters without varying their size distribution.



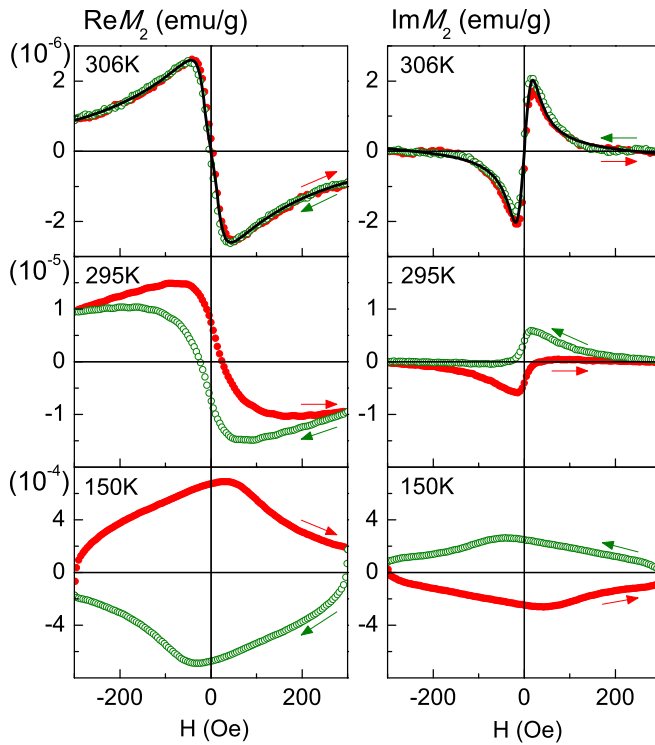


FIG. 8. Real (left panels) and imaginary (right panels) parts of the nonlinear magnetic response on the second harmonic for three characteristic temperatures: direct (solid red circles) and reverse (open green circles) scans with the fit for 306 K (continuous line); every tenth point is shown.

Such a behavior is rather a common trend. From the similar studies of doped manganites and cobaltites [32,39–41], two successive stages can be distinguished in the temperature evolution of FM clusters inside the paramagnetic phase: (i) At a certain temperature  $T^*$ , a small amount of clusters

emerge at structural inhomogeneities giving rise to a typical  $H$ -hysteretic irregular nonlinear magnetic response with extrema at weak dc fields. Upon cooling the signal amplitude and shape only slightly depend on temperature indicating invariance of the concentration of clusters. (ii) Below a certain temperature  $T^\# < T^*$ , rapid rise of the cluster signal begins, sometimes with a small hysteresis and distinct extrema at low dc fields, the shape of the signal remaining almost invariable. This regime corresponds to intensive increase of the concentration of clusters via homogeneous nucleation. The accumulation of clusters may be accompanied by redistribution of the cluster sizes toward larger ones [32]. As a rule, both  $T^\#$  and  $T^*$  do not exceed room temperature. The nonhysteretic signal at the highest measured temperature (Fig. 8) and the sharp rise of its intensity upon cooling (Fig. 9) manifest the sample to be already in the second stage of the cluster evolution with  $T^\# > 307$  K. The concentration of clusters observed in the sample at room temperature is reached in parent  $\text{Sm}_{0.5}\text{Sr}_{0.5}\text{MnO}_3$  at much lower temperature 120 K [14], in agreement with the neutron depolarization data (Fig. 7).

In the region 303–307 K, the signal from FM clusters was processed using the formalism based on the Fokker-Planck equation describing the kinetics of superparamagnetic particles [22,23] in the way it had been done in the study of MEPS in  $\text{La}_{0.85}\text{Sr}_{0.15}\text{CoO}_3$  [32]. From the simultaneous best fit for real and imaginary parts of the response (Fig. 8, upper panels), magnetic parameters of the SP system were evaluated. The main finding concerns the distribution of the cluster magnetic moments  $m$ . The elementary assumption on the log-normal distribution well agreeing with M2 data for  $\text{La}_{0.85}\text{Sr}_{0.15}\text{CoO}_3$  fails for  $\text{Sm}_{0.32}\text{Pr}_{0.18}\text{Sr}_{0.5}\text{MnO}_3$  as the fit procedure yields unrealistic parameters for this distribution. Instead, the power-law distribution  $\propto 1/m^\epsilon$  with the exponent varying from  $\epsilon = 2.6$  at 307 K to  $\epsilon = 2.9$  at 303.4 K well suits the M2 data. Thus, the cluster system is a volume fractal in the  $m$  range  $10^3$ – $10^9 \mu_B$  corresponding to the sizes from 10 nm to 1  $\mu\text{m}$ . However, the concentration of large clusters at these temperatures is too small to detect the long-range FM ordering by NPD.

The damping constant  $\alpha \simeq 1$  indicates predominately a thermal-diffusion scenario of the cluster magnetization dynamics with Larmor precession being almost suppressed. With the assumption of the uniaxial magnetic potential, the “easy-plane” anisotropy was identified. The anisotropy field  $H_a \simeq -20$  Oe is quite small as the real magnetic potential inside the clusters is close to cubic.

Upon further cooling, the cluster response continues to increase exponentially but at much slower rate (Fig. 9). At the same time, at  $T = 300$  K a magnetic hysteresis appears in the signal and increases on cooling as exemplified in Fig. 8 (panels 295 K). These features evidence the growth of clusters via coalescence while the accumulation of new clusters via homogeneous nucleation still goes on. At 250 K a part of the clusters become large enough to exhibit a long-range FM order in the NPD measurements (Fig. 5).

The temperature dependence of the “coercive force” defined as  $\text{Re}M_2(H_{C2}) = 0$  is given in the inset of Fig. 9 together with the extrema positions of  $M_2$  for real and imaginary parts. At 200 K ( $T_{PS}$ ) the increase of  $H_{C2}$  upon cooling becomes steeper indicating enhancement of the cluster coalescence due

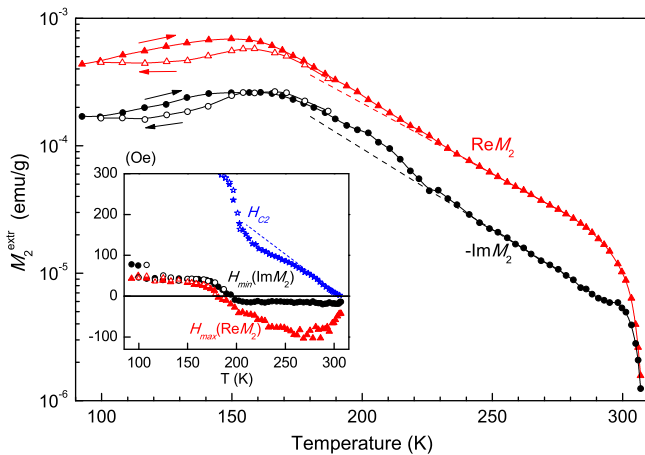


FIG. 9. Temperature dependencies of the extrema values of real and imaginary parts of M2 signals for the negative dc field region on cooling (open symbols) and warming (solid symbols). Inset: the “coercive force”  $H_{C2}$  and extrema positions of the real ( $H_{\max}$ ) and imaginary ( $H_{\min}$ ) parts vs temperature. Broken lines are guides for the eye visualizing deviations from linearity.

to intake of electrons from the arising phase II [Fig. 3(b)]. The “coercive force” is a measure for the phase lag of the response from the scanning dc field depending on the ratio of the relaxation time of the cluster system to the scan period of the dc field 0.125 s. The relaxation time rises on cooling approximately as  $\exp(mH_a/T)$ . In turn,  $m$  intensively grows via coalescence. These tendencies jointly yield the rapid, singularity-like increase of the “coercive force” indicating the blocking of the cluster magnetic moments as the clusters reach macroscopic sizes. Besides, at this temperature the large clusters come in broad contact with the crystallite boundaries which provokes pinning of their magnetic moments. The blocking of magnetic moments reveals itself also in the temperature behavior of positions of the signal extrema (Fig. 9, inset). At 180 K both  $H_{\max}(\text{Re}M_2)$  and  $H_{\min}(\text{Im}M_2)$  change their signs embodying strong distortions of the hysteresis curves as seen in Fig. 8 (bottom panels 150 K). The accumulation of a considerable amount of large FM clusters is a prerequisite for forthcoming percolation.

A similar temperature behavior of the “coercive force” was observed also in  $\text{Sm}_{0.5}\text{Sr}_{0.5}\text{MnO}_3$  with the blocking of magnetic moments somewhat below 120 K [14].

At 150 K, on the eve of percolation, the coalescence saturates and the  $M_2$  response reaches its maximum (Fig. 9). The neutron beam polarization ceases to decrease and the neutron refraction on magnetic boundaries also tends to stabilize (Fig. 7). The  $M_2$  temperature hysteresis below 160 K manifests the onset of percolation of FM clusters inside the phase I crystallites. The hysteresis well correlates with the similar temperature behavior of the zero-field resistivity (Fig. 6).

Gradual decrease of the  $M_2$  response below 150 K (Fig. 9) is driven, mainly, by two tendencies, viz., (i) the magnetic homogenizing of phase I crystallites due to the spread of “infinite” FM clusters over the whole orthorhombic phase area, and (ii) the simultaneous decrease of this phase fraction. Below 100 K the temperature hysteresis closes, the whole phase I becomes ferromagnetic, and the evolution of PS, both crystalline and magneto-electronic, eventually finishes.

Below 150 K the  $M_2$  patterns remain qualitatively the same down to the lowest temperature 92.5 K.

The FM cluster evolution uncovered by  $M_2$  measurements is one more, even more robust, piece of evidence of the interphase electron transfer. It is this mechanism which favors rapid enhancement of the FM-cluster coalescence and enables clusters to reach their percolation and to stabilize the magneto-electronically phase-separated ground state, viz., the electron-enriched FM phase I (corresponding to the phase diagrams of SmSr and PrSr manganites [4] for  $x < 0.5$ ) and the electron-deficient AF phase II (corresponding to  $x > 0.5$ ). As the total number of electrons is fixed at the level  $x = 0.5$ , then, due to the charge conservation law, the initial concentration of electrons in phase I would not have been enough for its ground-state FM state while the surplus of electrons in phase II would have prevented occurrence of the stable AF order.

#### IV. CONCLUSION

The effect of isovalent substitution of rare-earth cations on the phase separation in half-doped manganites was studied on  $\text{Sm}_{0.32}\text{Pr}_{0.18}\text{Sr}_{0.5}\text{MnO}_3$  using neutron powder diffraction, neutron beam depolarization, nonlinear magnetic response, and magnetization and conductivity measurements. The rare-earth cation IS enhances the PS tendency both in the structural and magnetic subsystems. Segregation of the monoclinic phase from the high-temperature orthorhombic phase was found to occur in the temperature region exceeding that of the parent compounds and to persist down to helium temperatures. The crystalline PS is accompanied by macroscopic magneto-electronic PS into FM structure in the orthorhombic phase and two AF structures of A and CE types in the monoclinic phase. Transfer of electrons from the monoclinic to orthorhombic phase on cooling stabilizes the respective magnetic orders in both crystal phases.

Microscopic magneto-electronic PS in the form of FM clusters in the paramagnetic matrix arises above the room temperature in the orthorhombic phase. The clusters coalesce upon cooling. The structural PS stimulates sharp enhancement of the cluster coalescence via the interphase electron transfer resulting in the percolative phase transition at low temperatures.

IS primarily implies only variation of the geometrical parameters such as the average cationic radius and the variance as opposed to the conventional doping with divalent ions additionally changing the concentration of charge carriers. Thus, the IS is a more delicate means of modifying the physical properties of transition metal oxides, PS vastly underlying these properties. This peculiar feature of IS is strongly highlighted in the vicinity of phase boundaries where the system is especially unstable with respect to PS. Half-doped manganites are one of the most relevant cases. The present study uncovered the essential effect of the rare-earth IS on PS in this particular case. The detailed characterization of this phenomenon is believed to contribute to elucidation of the mechanisms determining the relevant physical properties. More generally, strong electron correlations with the interplay of lattice, magnetic, and charge degrees of freedom at half doping underlie the peculiar character of the studied PS.

Finally, the question arises, which features of the studied phenomenon are generic for this type of IS and which of them are specific for the particular compound? To answer this question, a study of similar manganites with different combinations of rare-earth and alkali-earth cations is needed.

#### ACKNOWLEDGMENTS

The reported study was funded by the Russian Science Foundation according to Research Project No. 18-12-00375. The authors are grateful to the managements of PIK Data Centre and of Peter the Great Saint-Petersburg Polytechnic University Supercomputing Centre for making available the computational resources.

[1] E. Dagotto, T. Hotta, and A. Moreo, *Phys. Rep.* **344**, 1 (2001).

[2] R. Kajimoto, H. Yoshizawa, Y. Tomioka, and Y. Tokura, *Phys. Rev. B* **66**, 180402(R) (2002).

- [3] Y. Tomioka, H. Hiraka, Y. Endoh, and Y. Tokura, *Phys. Rev. B* **74**, 104420 (2006).
- [4] C. Martin, A. Maignan, M. Hervieu, and B. Raveau, *Phys. Rev. B* **60**, 12191 (1999).
- [5] A. Machida, Y. Moritomo, E. Nishibori, M. Takata, M. Sakata, K. Ohoyama, S. Mori, N. Yamamoto, and A. Nakamura, *J. Phys. Soc. Jpn.* **69**, 3536 (2000).
- [6] F. Damay, C. Martin, A. Maignan, M. Hervieu, B. Raveau, Z. Jirak, G. André, and F. Bourée, *Chem. Mater.* **11**, 536 (1999).
- [7] M. M. Savosta, A. S. Karnachev, S. Krupička, J. Hejtmánek, Z. Jiráček, M. Maryško, and P. Novák, *Phys. Rev. B* **62**, 545 (2000).
- [8] F. N. Bukhanko and A. F. Bukhanko, *Phys. Solid State* **58**, 519 (2016).
- [9] Z. M. Wang, G. Ni, Q. Y. Xu, H. Sang, and Y. W. Du, *J. Appl. Phys.* **90**, 5689 (2001).
- [10] A. Mleiki, S. Othmani, W. Cheikhrouhou-Koubaa, M. Koubaa, A. Cheikhrouhou, and E. K. Hlil, *J. Alloys Compd.* **645**, 559 (2015).
- [11] S. Shimomura, N. Wakabayashi, H. Kuwahara, and Y. Tokura, *Phys. Rev. Lett.* **83**, 4389 (1999).
- [12] A. M. Balagurov, V. Yu. Pomjakushin, D. V. Sheptyakov, V. L. Aksenov, N. A. Babushkina, L. M. Belova, A. N. Taldenkov, A. V. Inyushkin, P. Fischer, M. Gutmann, L. Keller, O. Yu. Gorbenko, and A. R. Kaul, *Phys. Rev. B* **60**, 383 (1999).
- [13] V. Yu. Pomjakushin, D. V. Sheptyakov, K. Conder, E. V. Pomjakushina, and A. M. Balagurov, *Phys. Rev. B* **75**, 054410 (2007).
- [14] A. I. Kurbakov, A. V. Lazuta, V. A. Ryzhov, V. A. Trounov, I. I. Larionov, C. Martin, A. Maignan, and M. Hervieu, *Phys. Rev. B* **72**, 184432 (2005).
- [15] T. Holstein, *Ann. Phys.* **8**, 325 (1959).
- [16] H. Kawano, R. Kajimoto, H. Yoshizawa, Y. Tomioka, H. Kuwahara, and Y. Tokura, *Phys. Rev. Lett.* **78**, 4253 (1997).
- [17] E. Pollert, Z. Jiráček, J. Hejtmánek, A. Strejček, R. Kužel, and V. Hardy, *J. Magn. Magn. Mater.* **246**, 290 (2002).
- [18] H. Yoshizawa, R. Kajimoto, Y. Tomioka, and Y. Tokura, *Physica B* **329–333**, 679 (2003).
- [19] F. Damay, C. Martin, M. Hervieu, A. Maignan, B. Raveau, G. André, and F. Bourée, *J. Magn. Magn. Mater.* **184**, 71 (1998).
- [20] V. Yu. Ivanov, A. A. Mukhin, V. D. Travkin, A. S. Prokhorov, and A. Balbashov, *J. Magn. Magn. Mater.* **258–259**, 535 (2003).
- [21] C. Autret, C. Martin, M. Hervieu, A. Maignan, B. Raveau, G. André, F. Bourée, and Z. Jirak, *J. Magn. Magn. Mater.* **270**, 194 (2004).
- [22] S. V. Titov, P.-M. Déjardin, H. El Mrabti, and Yu. P. Kalmykov, *Phys. Rev. B* **82**, 100413(R) (2010).
- [23] H. El Mrabti, S. V. Titov, P.-M. Déjardin, and Yu. P. Kalmykov, *J. Appl. Phys.* **110**, 023901 (2011).
- [24] V. V. Runov, D. Yu. Chernyshov, A. I. Kurbakov, M. K. Runova, V. A. Trunov, and A. I. Okorokov, *J. Exp. Theor. Phys.* **91**, 1017 (2000).
- [25] I. D. Luzyanin, V. A. Ryzhov, D. Yu. Chernyshov, A. I. Kurbakov, V. A. Trounov, A. V. Lazuta, V. P. Khavronin, I. I. Larionov, and S. M. Dunaevsky, *Phys. Rev. B* **64**, 094432 (2001).
- [26] A. I. Kurbakov, V. A. Trounov, A. M. Balagurov, V. Yu. Pomjakushin, D. V. Sheptyakov, O. Yu. Gorbenko, A. R. Kaul, I. I. Larionov, and S. M. Dunaevsky, *Phys. Solid State* **46**, 1704 (2004).
- [27] A. I. Kurbakov, C. Martin, and A. Maignan, *J. Phys.: Condens. Matter* **20**, 104233 (2008).
- [28] A. I. Kurbakov, C. Martin, and A. Maignan, *J. Magn. Magn. Mater.* **321**, 2601 (2009).
- [29] A. I. Kurbakov, V. A. Trunov, T. K. Baranova, A. P. Bulkin, R. P. Dmitriev, Ya. A. Kasman, J. Rodriguez-Carvajal, and T. Roisnel, *Mater. Sci. Forum* **321–324**, 308 (2000).
- [30] J. Rodriguez-Carvajal, *Phys. B (Amsterdam)* **192**, 55 (1993).
- [31] M. Halder, S. M. Yusuf, A. Kumar, A. K. Nigam, and L. Keller, *Phys. Rev. B* **84**, 094435 (2011).
- [32] A. V. Lazuta, V. A. Ryzhov, V. V. Runov, V. P. Khavronin, and V. V. Deriglazov, *Phys. Rev. B* **92**, 014404 (2015).
- [33] V. A. Ryzhov, I. I. Larionov, and V. N. Fomichev, *Tech. Phys.* **41**, 620 (1996).
- [34] E. C. Stoner, *Proc. R. Soc. London A* **165**, 372 (1938).
- [35] H. Böttger and V. V. Bryksin, *Hopping Conduction in Solids*, Physical Research (Akademie-Verlag, Berlin, 1985), pp. 51–65.
- [36] J. Lago, P. D. Battle, M. J. Rosseinsky, A. I. Coldea, and J. Singleton, *J. Phys.: Condens. Matter* **15**, 6817 (2003).
- [37] M. B. Salamon and M. Jaime, *Rev. Mod. Phys.* **73**, 583 (2001).
- [38] A. Maignan, C. Martin, M. Hervieu, B. Raveau, and J. Heitmanek, *Solid State Commun.* **107**, 363 (1998).
- [39] V. A. Ryzhov, A. V. Lazuta, I. D. Luzyanin, I. I. Larionov, V. P. Khavronin, Yu. P. Chernenkov, I. O. Troyanchuk, and D. D. Khalyavin, *J. Exp. Theor. Phys.* **94**, 581 (2002).
- [40] V. A. Ryzhov, A. V. Lazuta, P. L. Molkanov, V. P. Khavronin, A. I. Kurbakov, V. V. Runov, Ya. M. Mukovskii, A. E. Pestun, and R. V. Privezentsev, *J. Magn. Magn. Mater.* **324**, 3432 (2012).
- [41] V. A. Ryzhov, A. V. Lazuta, V. P. Khavronin, P. L. Molkanov, and Ya. M. Mukovskii, *J. Phys.: Condens. Matter* **26**, 076001 (2014).